SCA2025-xxx

Using Minkowski Functionals to Improve the Accuracy of Residual Gas Saturation (compressed air, CH4, H2) from µCT Core Flooding Experiments

Ying Gao[1*], *Tibi* Sorop[1], *Yingxue* Wang[2], *Karin* de Borst[1], *Niels* Brussee[1], *Hilbert* van der Linde[1], *and Steffen* Berg[1]

[1]Shell Global Solutions International B.V., 1103 HW Amsterdam, Netherlands,
[2]Shell Exploration & Production Company, Houston, Texas, USA

Abstract. Residual saturation is a key input parameter for modelling subsurface processes such as hydrocarbon (HC) gas production, gas injection, Water Alternating Gas (WAG) injection, as well as CCS and H_2 storage. Since pore scale gas dynamics is subject to a wider range of physical effects than immiscible and insoluble liquids, such measurements cannot be performed using a model fluid system but require a representative gas-liquid system. In low-rate unsteady-state (USS) core flooding, the method mostly used in the industry, factors such as gas compressibility and ripening-induced gas/brine dissolution can lead to a high degree of uncertainty in estimating relative permeabilities and residual saturation (Sgr), with negative impact on field development decisions.

To address this problem, in-situ high resolution X-ray micro-CT (µCT) imaging was used to monitor the pore-scale processes and Sgr during the flow experiments where gas-saturated brine displaced gas (compressed air/N_2, CH_4 and H_2). The experiments confirmed the impact of gas/brine dissolution, i.e., a continuous decrease in gas saturation the more brine was injected, beyond the expected values of Sgr. This occurred even though the injected brine was fully equilibrated with the gas, and continued ~~even~~ after the brine injection was stopped, because of an intrinsic effect in the porous medium related to Ostwald ripening. In gas-liquid systems, capillary equilibrium involves diffusive transport between disconnected gas clusters through a super-saturated liquid phase. Therefore, injecting (non-supersaturated) gas-saturated brine leads to dissolution of gas in the pore space, making it very difficult to determine Sgr.

A new approach is proposed in this paper, where pore scale flow regimes are characterized by fluid topology, i.e., Minkowski functionals computed from the in-situ pore scale imaging. The transition from displacement to trapping dominated regime is characterized by the Euler characteristic reaching a stable value and the onset of the dissolution regime is characterized by the moment the interfacial area starting to decrease.

In the dissolution-dominated regime, the dissolution rate is gas-specific, and it scales with Henry's constant times the diffusion coefficient. In the final trapping state, there are systematic differences in Sgr between the gases studied, with CH_4 and H_2 showing higher Sgr than compressed air/ N_2. This has potentially significant implications: 1) as most of the Sgr and gas/water relative permeabilities are measured in the laboratory using compressed air/N_2 and therefore it may imply that at least some of those experiments and results may need to be revisited; 2) as Sgr is the key parameter on recovery and/or storage in modelling.

Commented [FN1]: Characterized by the moment the interfacial area starts to decrease , you mean ?

Commented [YG2R1]: This is addressed

1 Introduction

Many subsurface engineering applications involve the transport of one or more liquid phases and a gas phase. Examples range from the underground storage of carbon dioxide (CO_2) and hydrogen (H_2) [1-4], the recovery of natural gas. For these applications, for assessing and optimizing the efficiency it is important to estimate the residual gas saturation (Sgr) [5-7] with respect to an aquifer. For instance, the Sgt for trapped gas saturation (which is the trapped saturation after the aquifer re-imbibes) is a direct measure of how much CO_2 can be stored at a specific site. For the underground storage of H_2, Sgr influences the H2 recovery of cyclic injection and withdrawal. For natural gas production, the trapped gas saturation Sgr is a direct measure of how much gas can be produced from a gas reservoir that is in contact with an active aquifer. The trapping process consists of imbibition of the wetting aqueous phase which involves capillary processes such as snap-off which then leads to disconnection of the non-wetting gas phase and capillary trapping.

* Corresponding author: Y.Gao3@shell.com

Sgr is an important factor to estimate the overall efficiency of the aforementioned processes and associated economics of the projects. Sgr is often ranking top-5 in the sensitivity assessment for stored/recovered gas volumes, which is the subsurface basis for commercial contracts, dimensioning of infrastructure and more.
Since the residual gas saturation Sgr depends (besides many other parameters such as initial water saturation) on the rock, much attention is given to determining Sgr for the specific reservoir rocks in the laboratory using core analysis and special core analysis (SCAL). However, Sgr is notoriously difficult to determine within an acceptable uncertainty range. Over the past decade, many experiments conducted by different laboratories have reported a wide uncertainty range from 5 - 60%, even for similar rocks with similar porosity and permeability [8-18]. But this not explainable alone from differences in pore structure. The large uncertainty range which is statistically robust against outliers suggests that there are parameters or phenomena in gas-SCAL which are not sufficiently understood and controlled. A research team led by Cense [7] has identified dissolution of gas during the gas-SCAL experiment as a key source of uncertainty. Typically, in order to determine Sgr, a large number of pore volumes of brine need to be injected until all displacement processes have ceased and the trapped, true residual Sgr can be determined. For that purpose, the injected brine is pre-equilibrated with the gas, to avoid any dissolution. Despite all meticulous efforts to pre-equilibrate the gas across laboratories in industry and academia, still gas started dissolving before Sgr was reached [7]. The experimentally determined Sgr was significantly affected by an undesired dissolution process [5-7]. In order to address this question, in this study further evidence is provided for the ripening hypothesis and more experimental data is gathered for a wide range of gas-liquid systems including compressed air (mainly N_2), CH_4 and H_2) [25-28].

The dissolution process, which was always classified as an experimental artefact, was not clear, nor was it understood what the cause of dissolution was [7-24]. The effort to pre-equilibrate the brine with gas is credible and obvious mistakes there can be ruled out [7]. This leaves us with the possibility of an in-situ process in the porous medium specific to gasses. X-ray computed tomography provides increasing insight into in-situ pore scale processes [19,20] such as the displacement and dissolution dynamics of gas/oil/water systems at the scale of individual gas bubbles within the pore space of reservoir rock [19,21]. Over the past decade, micro-CT has been used for instance to study the trapping of CO_2 [22, 23] and assess for instance the impact of wettability [24]. While initially the time resolution in such micro-CT core flooding experiments was only sufficient to capture initial and end states, more recently the time resolution has been increased to study dynamic processes [25-27]. While most of these experiments considered mutually equilibrated gas-liquid phases as a system analogous to immiscible liquids, the groundbreaking work by Ke Xu and co-workers [34-35] has made clear that a gas-liquid system can be fundamentally different than liquid-liquid system. The reason is that immiscible liquid-liquid systems are largely mutually insoluble, while for gasses there is always as significant degree of solubility. This leads to ripening effects which in a porous medium are more complex due to the geometric confinement of the pore space which leads to additional complexity [34-35]. While initially mainly conducted in 2D micromodels [34-35], two studies in our group have demonstrated ripening in 3D pore geometries in hydrocarbon liquid-gas systems but also in gas-brine systems [36-37]. This is confirmed by other research groups by numerical modelling [41-42] and experimentally [43-45]. Ripening falls into the wider class of processes where – similar as nucleation of gas bubbles – the gas concentration in the liquid in pore space can exceed the mutual phase equilibrium outside of the porous medium, i.e., become super-saturated [17]. Previous studies have suggested that the super-saturation associated with the phase equilibrium for gas-liquid systems inside the pore space subject to ripening and anti-ripening may contribute or even explain the effect of gas bubbles dissolving even though injected fluids are mutually saturated [30]. In essence, fluids are only mutually equilibrated at injection pressure conditions, while the phase equilibrium inside the porous medium is at injection pressure plus the capillary pressure associated with the gas bubbles. Therefore, from the perspective of in-situ condition inside the porous medium the injected fluids are under-equilibrated which leads effectively to gas dissolution.

This hypothesis would support the view that the dissolution effect is indeed an experimental artefact. However, this artefact cannot be avoided in core flooding experiments, because it is not so straight-forward or might even be impossible to inject at porous media phase equilibrium level, which would be super-saturation at injection conditions. Furthermore, since the capillary pressure increases during the displacement and reaches a stable high level at trapping conditions, the equilibration level would need to be adjusted dynamically.

Therefore, the real problem when determining Sgr seems to be that it is not possible to discriminate displacement (i.e. trapping) effects leading to Sgr and dissolution effects from ripening, which start impacting the Sgr measurement. In other words, a methodology is needed that allows to discriminate the displacement regime (and the Sgr at the end of the displacement regime) from the ripening/anti-ripening dominated dissolution regime.

There are two objectives of this study: (i) confirm that dissolution is affecting saturation profiles (and, thus, Sgr) during coreflooding experiments and clarify the underlying physical processes, (ii) identify a post-processing approach that enables to discriminate between dissolution and displacement regimes and that enables to derive reliable Sgr values.

2 MATERIALS AND METHODS

2.1. Rock properties

A cylindrical sample of Bentheimer sandstone rock with the diameter of 4 mm and length of 20 mm was used in this study. The porosity estimated from the micro-CT image was 20.4 %. The permeability measured on the bulk plug, from which this mini-plug was drilled, is 2,513 mD (2.48×10^{-12} m^2). Most of the pores are larger than 10 µm, which means that a 5 µm resolution of the scanner is good enough to capture the behaviour of liquid and gas fluid phases in the pores. Note that the sample was drilled to a diameter of 4 mm, which is significantly smaller than the typical core-plug samples (of either 1 inch or 1.5 inch in diameter), to enable access to the highest resolution of the micro-CT scanner. This is also in line with other Digital Rock flooding experiments performed in industry or academia.

2.2 Fluid properties

The brine used in this study is using 5 wt% NaI brine to increase the contrast and to distinguish the interface between gas and brine. The gasses used in this study were either compressed air, methane (CH4) or hydrogen (H2). The experimental condition is room temperature, and the back pressure is 5 bar.

Table 1. Gas properties at the same conditions at 20 ºC and 1 atm

Gas	Density [kg/m^3] @20ºC	Viscosity [cP]@20ºC	Diffusion coefficient [cm^2/s]
Compressed air	1.204	0.0181	0.219
N_2	1.164	0.0176	0.176
CH_4	0.668	0.0110	0.219
H_2	0.0828	0.0087	0.61

3 Experimental and imaging methods

3.1 Experimental methods

Unsteady state (USS) corefloods with brine displacing gas experiments were conducted at laboratory temperature conditions. The study was conducted as follows: a) an USS flow experiment using compressed air fully saturated brine (the brine was gas-saturated prior to the start of the experiment); b) an USS flow experiment performed using unsaturated (gas-free) brine; c) an USS flow experiment using CH4 fully saturated brine; d) an USS flow experiment using H2 fully saturated brine; and e) repeat experiment d).

The experimental flow apparatus comprises three main components: core holder, differential pressure transducer, and pumps (to apply a constant flow rate as well as maintaining a constant confining stress and back pressure), shown in Fig. 1, as it has been described in ref [30]. The sample was placed in a fluoropolymer elastomer (Viton) sleeve in the carbon fibre Hassler type flow cell. Fluid flow lines were used to connect the core holder with the pumps. Only air was inside of the rock sample at the start of the experiment, meaning that the initial gas saturation is Sg = 100%. Before the displacement, brine and gas were mixed by recirculating through the flow lines, bypassing the sample at 5 bar, for more than 48 hours to make sure the brine was fully gas saturated. Then gas saturated brine was injected at a (constant very low flow rate, of 0.5 µL/min, to ensure that the pressure drop across the sample is less than 2% of the pore pressure (as recommended in Cense et al. [7]) to minimize the potential gas compressibility effects. Images with voxel size of 5 µm were taken at the same time continually during the coreflooding. It usually takes around 30 minutes for a high-resolution 3D image. More details can be found in Gao et al. [30].

Commented [FN3]: How exactly did you perform the gas saturation of the brine ? It lacks an explanation of the method and maybe if possible an illustration of the set-up.

Commented [YG4R3]: Key procedures and the set-up have been added. More details can be found in reference [30] .

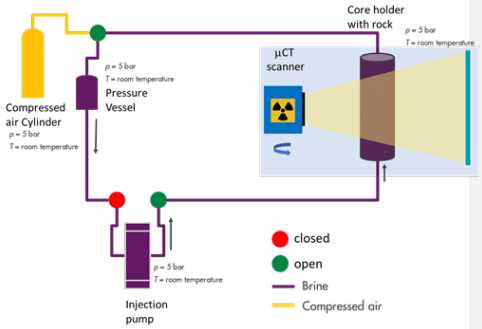

Fig. 1. The experimental flow apparatus used in this work.

3.2 Imaging methods

Dynamic core flooding experiments with in-situ pore-scale 3D imaging were performed using a DynaTOM (TESCAN) micro-CT scanner with a vertical gantry. The 2 cm long (and 4 mm diameter) mini-core was scanned at a resolution of 5 µm in 4 segments, which were stitched together to a 800 × 800 × 3780 voxel image – shown in Fig. 2. The scans were performed at 130 kV and a power of 16 W, and 1500 projections. For dry scans a 10 frame-averaging was used to improve signal-to-noise level for the pore space segmentation. Dynamic scans were performed with only 1 frame, resulting in a scan time of 30 min for the whole 2 cm long section.

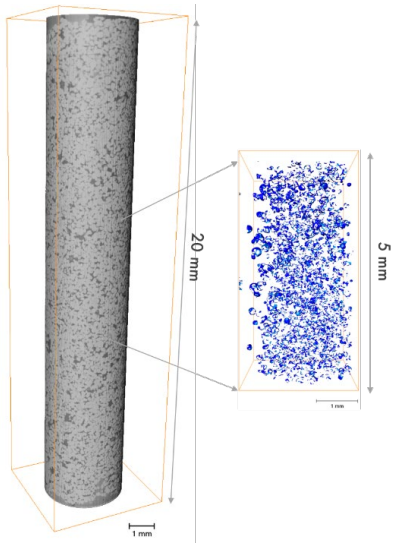

Fig. 2. On the left, the stitched three-dimensional X-ray image of the whole sample used in the experiment, with voxel size of 5 µm. On the right, gas-brine interface extraction based on three-phase segmentation.

The image processing workflow consisted of (1) segmentation of the pore space from the dry scan, (2) registration of the dynamic scan grey level images on the dry scan (using Lanczos resampling [31]), (3) filtering with a non-local means filter [32], (4) applying the dry segmentation as a mask for the pore space and (5) segmenting the gas-liquid phases in the pore space with a watershed based method using Avizo (ThermoFisher). The cross-section images of the sample are shown on the left in Fig. 3. The middle image shows the segmented image of the dry scan, pore space in blue and grains in grey. The right image shows the segmented image when 25.6 PV brine was injected, with brine in blue, gas in red and grains in grey.

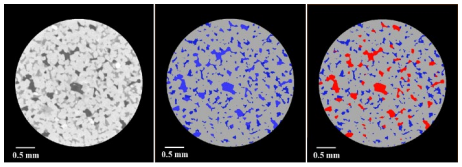

Fig. 3. Two-dimensional cross sections of three-dimensional segmented images of a dry scan (left). The right one shows the same slice for a flow experiment with the gas phase in red and brine in blue.

4 Results

The results of the 5 experimental tests are combined in a single plot, shown in Fig. 4, of average water saturation (Sw) over the whole sample, as a function of PV brine injected. As described in detail in Ref. [30] for brine/compressed air displacement, we find a similar behaviour for the experiments where the gas-liquid systems are mutually saturated at injection conditions. There are two main flow regimes:

(1) Displacement-dominated regime (early)
(2) Dissolution-dominated regime (late)

At early time there is predominantly the displacement-dominated regime present, while at late times the dissolution-dominated regime is present. These regimes overlap in-between, and from the saturation-vs-PV-injected plot in Fig. 4 it is not clear where displacement ends and where dissolution starts. For the intentionally under-saturated compressed air experiment the overlap between regimes is significant and we hypothesize that also at the pore scale displacement and dissolution occur nearly simultaneously over most of the mobile saturation phase. For the mutually equilibrated cases the overlap between regimes seems to be much less, which suggests that a discrimination may be possible. But saturation alone is not sufficient to distinguish regimes. More information from pore scale gas configurations may be required.

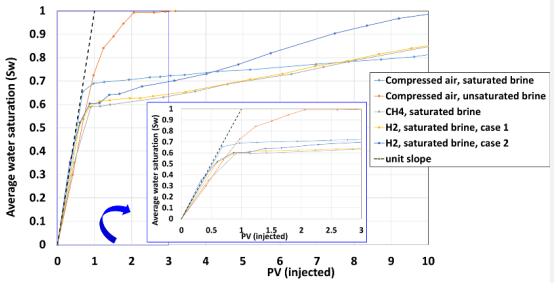

Fig. 4. Water saturation measured of the 5 USS G/W experiments.

Commented [FN5]: Please, add the legend of the black dotted line (slope 1). Specify also somewhere in the graphic that the small illustration is a zoom on the 3 first PVs.

Commented [YG6R5]: This is addressed

To be more specific of how the dissolution happens in the pore space, 3D images of the configuration of gas along the sample during the USS flow experiments are shown in Fig. 5 for the Hydrogen case I as an example. We can see that the gas was displaced out of the sample for the first 1-2 PV of injection and the remaining gas was trapped inside of the pore space. After about 1.5 – 2 PV of injection, gas started to dissolve into the brine from the inlet until all gas fully dissolved. The saturation profiles along the cores were computed for this experiment, as shown in Fig. 6. From the segmented 3D images the saturation in each slice perpendicular to the long sample axis was averaged and plotted vs. distance from the inlet, Sw increased from 0 to around 0.6 when the brine saturation reaches a stable Sw relatively uniformly across the sample after the injection of 1-2 PV, leading to significant trapping, which is related to the displacement stage. After several PVs are injected in the sample, the gas phase starts to disappear from the inlet i.e. as a frontal

dissolution process, commencing what we call the dissolution dominated phase. However, we still see some homogeneous increase of saturation during that stage in a similar manner as during the displacement stage which could indicate that during this stage still displacement occurs. The dissolutions occur until gas saturation locally decreases to 0.

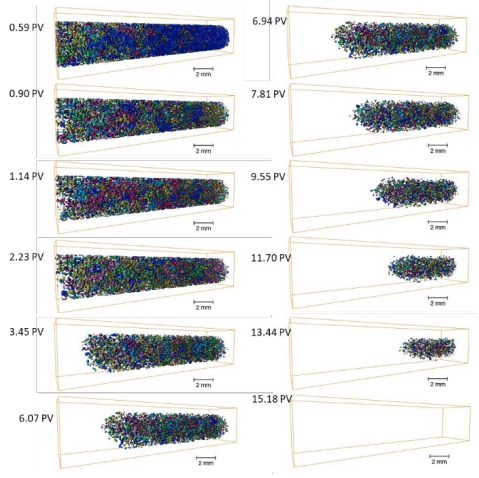

Fig. 5. Three-dimensional images of the configuration of gas along the sample during the USS flow experiment with Hydrogen. Each colour represents separated gas clusters/ganglia.

From the coreflooding experiments performed with various gases and at different conditions presented in Section 3, we have concluded that there are two distinct flow regimes:

- a displacement dominated regime -- characterized by a quick decrease of gas saturation (i.e. steeper slopes in Sg vs. PV injected plots), and
- a dissolution dominated regime -- characterized by a slower decrease of gas saturation (i.e. less steep slopes in Sg vs. PV injected plots).

These are illustrated in Fig. 4. In some cases (see the displacement by fully saturated brine), the displacement and dissolution regimes are – to some extent - clearly separated, resulting in an initial slope of around 1. In other cases, however, the regimes are overlapping, as shown, for instance, the orange curve in Fig. 4, which is the case displaced by the unsaturated brine.

To confirm our hypothesis of a displacement-dominated regime followed by a dissolution-dominated regime, in Fig. 7 we plot for the dissolution-dominated regime the dissolving gas fraction (by subtracting the presumably trapped, which is the saturation when gradient of the production plot decreases) as a function of injected pore volumes of brine. We observe distinct differences in dissolution kinetics between different gases which is expected. We can see that after injecting around 1 PV brine, the gradient of each curve is different, where the absolute value of the gradient of H_2 is largest, that of CH_4 is less, and that of compressed air is the lowest. This is because the dissolution depends on solubility and diffusion coefficient is for each specific gas. The slope of the dissolution kinetics then forms a linear trend with the Henry constant KH (representing the solubility) and the diffusion coefficient D for the respective gasses, i.e. KH·D [33] listed in Table 2, see Fig. 8. The fact that the 2nd regime can be reconciled against KH·D supports the view that this is indeed the dissolution regime.

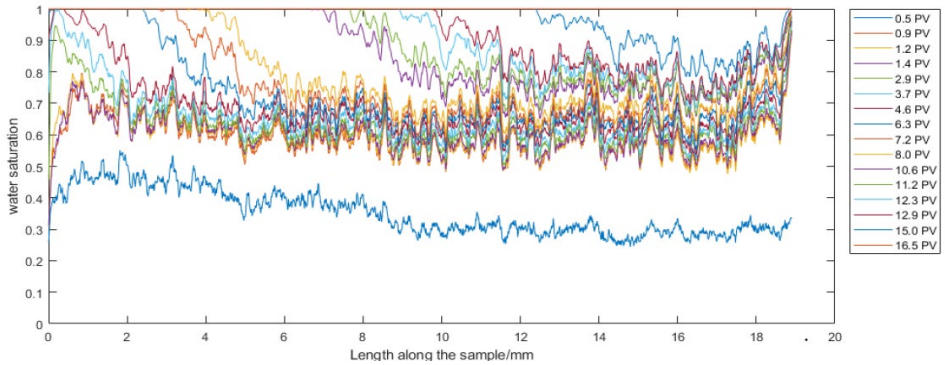

Fig. 6. Manifestation of the (anti)ripening-induced dissolution which begins at the inlet where the water saturation increases to 100% as all trapped gas is successfully dissolved. There is, however, no clear discriminator in the saturation data when displacement stops and where dissolution begins.

Commented [FN7]: What criteria tells you that the dissolution regime starts just after the breakthrough and not some amount of PVs after breakthrough?

Commented [YG8R7]: Indeed, it can not be separated that sharp. When the brine is fully gas saturated, the slope of the displacement regime is around 1.

Commented [FN9]: Orange ?

Commented [YG10R9]: This has been addressed.

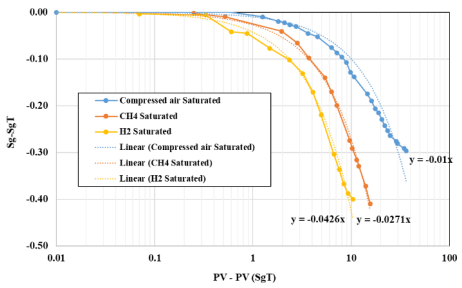

Fig. 7. Gas saturation in the dissolution regime: The fraction of dissolving gas Sg-SgT (where SgT is the trapped gas, where the Sg at the first point after approximately 1 PV brine injection indicates the end of gas displacement) as a function of the PV of brine injected.

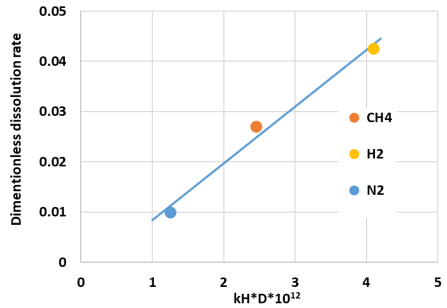

Fig. 8. The slope of the curves of the 2nd regime in Fig. 7 as a function of the dissolution regime of each gas.

Table 2. Henry's solubility constant

Gas	H_2/compressed air	H_2/CH_4
kH*D ratio	3.27	1.67
Slopes ratio	3.73	1.55

***Pure gas Henry coefficient in water**

Gas in water	Compressed air	H2	CH4
KH @ 25°C mol/(kg·bar)	7.5×10^{-4}	7.8×10^{-4}	1.4×10^{-3}

5 Discussion

5.1 Underlying Physics: Ripening and anti-ripening

The observation of a dissolution-dominated regime raises the question whether the dissolution is an experimental "mistake". While the utmost care has been taken in the present study, many studies published in the literature [7] makes such an obvious "mistake". For instance, in absence of an in-situ gas concentration measurement one could argue that full gas saturation of the brine has not been achieved. However, for the control experiment where on-purpose under-saturated brine has been injected, different production curve and saturation profiles have been observed. In other words, if the injected brine had not been nearly fully gas-saturated, we would be able to detect that. Therefore, we can rule out between an externally controllable "mistake" such as the under-saturation of the injected liquid. However, other experimental artefacts including unavoidable intrinsic effects such as ripening can still impact the experimental observation making the interpretation more complex.

As discussed in [34-35] ripening is an effect observed for two or more fluid phases with some degree of mutual solubility. The classical Ostwald ripening is encountered for many systems ranging from emulsions to crystals in ice cream and also gas bubbles. In essence, due to a dependency of solubility on capillary pressure and hence the size of bubbles, larger bubbles tend to grow while smaller bubbles (with higher capillary pressure) shrink. Ripening also occurs in porous media and will likely be present as soon as gases are involved (for which there is always solubility) [34,35]. Ripening has been observed in our previous study performed on hydrocarbon gas-liquid measurements, following a similar experimental methodology [29,30,36].

The experiments provide multiple supporting evidence that ripening is present here, as well:

1. Injected liquid is only saturated, not super-saturated
2. Dissolution begins from the inlet
3. Dissolution occurs, even though the injected liquid is fully gas-saturated
4. There is evidence from the previous work that ripening means diffusive exchange between trapped gas via super-saturation in liquid in-between [36]

In essence, the dissolution regime observed here is related to the fact that even though the injected liquid is fully saturated with gas outside the porous medium (at relevant injection pressure conditions), the mutual saturation equilibrium inside the porous medium is determined by injection pressure plus the capillary pressure. Furthermore, diffusive exchange between gas clusters requires a certain degree of super-saturation. Therefore, with respect to the equilibrium inside of the porous medium and the super-saturation required for gas exchange, the injected liquid is under-saturated in gas. In the terminology of the work of Xu et al. [34], this would then be the anti-ripening effect. That is unavoidable for each experiment because super-saturation outside of the porous medium would require different pressure or

Commented [FN13]: One could also argue that between two levels of undersaturated brines, the speed of the kinetic would be different. What if your «fully saturated brine» is finally «nearly full saturated brine» thus still undersaturated ?

Commented [YG14R13]: This has been addressed

Commented [FN11]: How do you identify the SgT?

Commented [YG12R11]: SgT is the trapped gas, where the Sg at the first point after approximately 1 PV brine injection indicates the end of gas displacement

temperature conditions, which then would not be compatible with the conditions inside the porous medium.

On the other hand, a proper understanding of the effect of dissolution due to anti-ripening would open the route for differentiating displacement and dissolution on the basis of pore scale descriptors. Dissolution would have an expected characteristic behavior in volume, surface area and connectivity. Dissolution would mean reduction of volume and impact of surface area, in particular when there is no connectivity. Displacement, on the other hand, would require connectivity. On this basis, a new methodology is proposed below.

5.2 Differentiating regimes with Minkowski functionals

In the following a new workflow is devised that aims at discriminating the (anti)ripening-induced dissolution regime from the displacement regime with the purpose to identify within an acceptable uncertainty range the end of the displacement regime and the associated residual gas saturation Sgr. The new workflow is based on utilizing the in-situ micro-CT imaging of the whole dynamic process to a larger extent than previously done. From the saturation data we have deduced that there are mainly two stages during the unsteady-state water-gas core flooding experiment: displacement – the gas phase was connected from inlet to outlet initially and then was trapped inside of pore space; this is a process that the number of gas clusters and ganglia are increasing, and dissolution – the size of the gas clusters/ganglia is decreasing and becoming more and more spherical, but the number of gas clusters/ganglia does not change quickly, which is shown in Fig. 9.

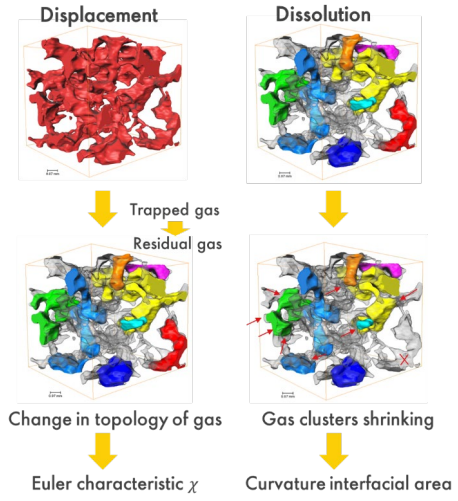

Fig. 9. Difference between displacement and dissolution. Displacement *mainly* affects the fluid connectivity, quantified through the Euler characteristic χ, while dissolution (indicated with red arrows) affects *mainly* interfacial curvature and interfacial area.

By utilizing the Minkowski functionals which have been identified as capillary state function [37], as morphological descriptors, the behavior from Fig. 9 can be quantified. In three dimensions there are 4 Minkowski functionals:

(1) volume (saturation)
(2) Interfacial area, the area between gas and water phase
(3) mean curvature $\kappa = (\kappa_1 + \kappa_2)/2$, with two principal curvatures κ_1 and κ_2 (related to capillary pressure)
(4) the Gaussian curvature $\mathrm{K} = \kappa_1\kappa_2$ which is related to the Euler characteristic χ .

The Euler characteristic can be used to distinguish whether the number of the gas bubbles/clusters changes, or their connectivity. Interfacial area can be used to check how quickly clusters dissolve. The gas ganglia shape is becoming more and more spherical, which could be reflected by the (mean) curvature. Fig. 9 illustrates the basic idea to discriminate flow regimes using the Euler characteristics, interfacial area and mean curvature.

5.3.1 Connectivity: Euler characteristic

The Euler characteristic is a topological invariant. It can be expressed as the alternating sum of the Betti numbers [38,39]

$$\chi_i = B_0 - B_1 + B_2 \qquad (1)$$

where B_0 is the number of connected components, B_1 is the number of loops and B_2 is the number of cavities enclosed within the object (which is not relevant for this application). Fig. 10 shows the Euler characteristic of simple shapes.

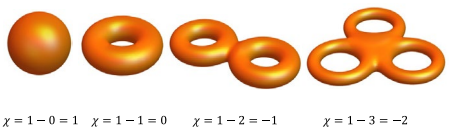

Fig. 10. The Euler characteristic χ of simple shapes

Fig. 11 shows how the Euler characteristic of the gas clusters changes during the process of the USS G/W experiments. At the start of the experiment, because the gas phase is connected from the inlet to outlet and the pore space is very complex with loops, the Euler characteristic is a very large negative number. With more brine injected, gas started to be trapped in the pore space and the number of the disconnected component was increasing while the

number of the loops is decreasing. Therefore, the Euler characteristic was increasing. By the end of the displacement regime, the Euler characteristic is positive. When the dissolution started to dominate, the number of the connected gas clusters/ganglia did not change until the small bubbles were eaten. With more gas bubbles disappearing, the Euler characteristic started to decrease to 0.

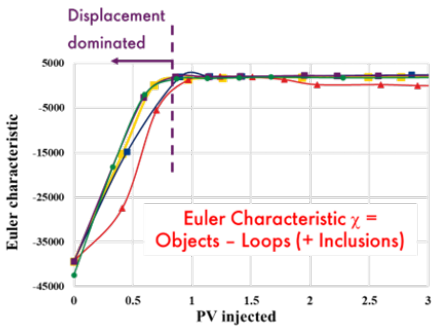

Fig. 11. Euler characteristic as a function of PV of brine injected for all 5 USS experiments.

5.3.2 Interfacial Area

Fig. 2**Error! Reference source not found.** shows the oil/brine interfaces at the middle of the sample for an image of size 500 × 500 × 1000 voxels with a voxel size of 5 μm as an example. The interface between oil and brine were extracted and smoothed using a volume preserving Gaussian smoothing to remove voxelization artefacts [40]. We can see that the interfaces are quasi-spherical when gas is trapped in the pore space.

We calculated all the interfacial area of the 5 experiments and the results are shown below in Fig. 12 bottom figure. At around 1 PV of brine injection, the interfacial area reached a plateau and later decreased because of dissolution until all gas dissolved.

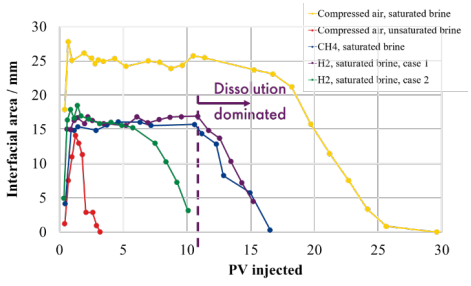

Fig. 12. Interfacial area calculated as a function of PV of brine injected for all 5 USS experiments.

5.3.3 Curvature of liquid-liquid interfaces

As mentioned in the last section, the interfaces are quasi-spherical in the water-wet case. The capillary pressure created because of the interface between gas and brine adds to the resistance to flow. At the first stage of displacement, there is only limited interface at the inlet of the sample. With more brine injected, more dissolution happens, and the interface between the gas and water is becoming more and more spherical, as shown in Fig. 13. The curvature of each point is calculated and shown in the plots at the bottom of Fig. 13.

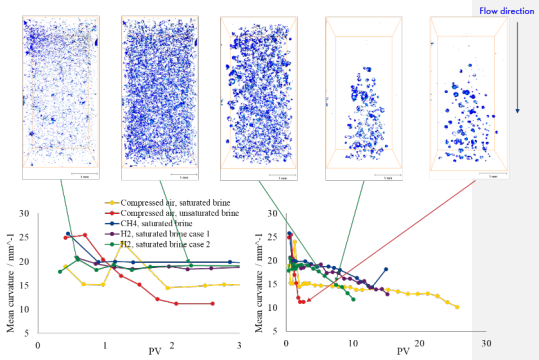

Fig. 13. Curvature analysis of the 5 USS G/W experiments.

5.3.4 Upper and lower bounds on the trapped/residual gas saturation

As we can see from the Euler characteristic, interfacial area and curvature analysis, both displacement-dominated and dissolution-dominated regimes show distinct trends. This confirms that Minkowski functionals can be used to differentiate the displacement and dissolution regimes, which can help to estimate the upper and lower bounds on the trapped/residual gas saturation.

Error! Reference source not found. As shown earlier, Fig. 11 shows the Euler characteristic, and Fig. 12 shows the interfacial area as a function of the pore volume of brine injected of all the 5 USS experiments.

- Upper limit to Sgr: end of displacement

The Euler characteristic starts from a large negative number because the gas in the rock sample is connected from inlet to outlet. The number increased once the brine injected as gas phase starts to disconnect and trapped in the pore space.

- Lower limit: beginning of dissolution-dominated regime

Interfacial area increased first because there was initially all gas inside. Then the interface area increases when brine started to inject into the sample. When dissolution starts, the interfacial area decreases.

As a conclusion, the end of the displacement-dominated regime provides an upper limit to Sgr while the beginning of dissolution-dominated regime provides a lower limit to Sgr.

That supports the view that the gas-saturated brine must really be at bulk saturation level, i.e. saturation at injection pressure (and temperature). However, in the pore space, that brine is slightly under-saturated with respect to the pore pressure of the gas, which is the injection pressure plus the capillary pressure of the gas. The situation is like ripening dynamics, where local capillary pressure leads to an increase in partitioning of gas into the liquid phase followed by diffusive transport to larger gas bubbles with lower capillary pressure. In absence of external flow, this diffusive exchange leads to the ripening dynamics. As the size of the gas bubble decrease because of the dissolution, the capillary pressure increases which is increasing the dissolution rate.

Previous studies indicated that ripening/anti-ripening processes occur indeed in gas-liquid systems [29,30,34,35]. Generally, this provides a credible setting for the effect observed here as well. The only difference here is that there is an external flow, while this is not included in the situation of previous studies. As we established in Fig. 7 and Fig. 8 there is no conceptual difference between the type of fluid, it is only a matter of solubility and diffusion coefficient. The presence of external flow implies that there is less chance of the traditional ripening to occur where smaller gas bubbles are "eaten" up by larger gas bubbles because that require local super-saturation and diffusive exchange. In these experiments with external flow, the mass exchange between small and large bubbles normally seen in Ostwald ripening is there but constrained.

5.3. Differences in Sgr between gases

We applied the new method based on Minkowski functionals, to compare the trapped gas saturation between compressed air, CH_4 and H_2.

In Fig. 4, we are showing the results of the 5 experimental tests combined in a single plot, of average water saturation (Sw) over the whole sample, as a function of PV brine injected, focusing on the first 3PVs. For case #2, of unsaturated brine displacing compressed air, water saturation increased very fast gas and, as expected, makes it almost impossible to define an accurate Sgr. Therefore, we will further focus on the other 4 experiments in which fully saturated brine was injected to displace compressed air, H_2 and CH_4.

Fig. 14 shows the trapped gas saturation, extracted using the Minkowski functionals method, for those 4 experiments. We observed that Sgr of H_2 is very close to that of CH_4, but both are higher than Sgr of compressed air.

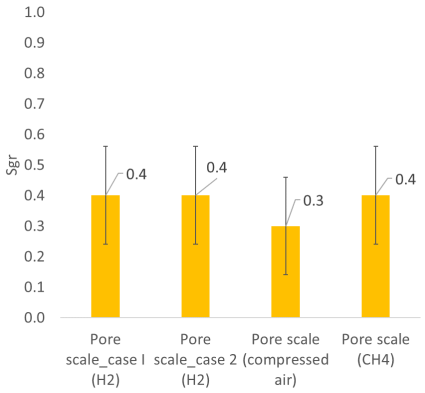

Fig. 14. Sgr of the 4 experiments when brine was fully saturated with gas.

This is an important finding, suggesting that H_2 behaves in a similar way to CH_4, while both show larger trapping values than compressed air. We do not know whether this is a result that is specific to this sample (we have used in all experiments the same high permeability Bentheimer sandstone) or it is generally valid. We, therefore, recommend, further investigations on different type of samples (carbonates, samples with clays, reservoir samples etc.). Moreover, these experiments were performed on mm-size samples, and it is not fully understood currently in the industry and academia, whether the results obtained with such small-sized samples are always representative ofthe reservoir scale (potential reasons: representative elementary volume etc.).

6. Conclusions

This work introduces a new method to determine the trapped gas saturation at pore scale, using the latest developments in Digital SCAL, and combining different Minkowski functionals (Euler characteristic, interfacial area and curvature analysis) to estimate and provide limits of the trapping saturation in a more objective manner. An experimental workflow combining state-of-the art imaging techniques and coreflooding opens the possibilities to capture time-lapse fluids distribution inside of rock dynamically. In contrast to the conventional in-situ saturation monitoring approach, used currently by many SCAL laboratories, this approach has the advantage that the dynamic behaviour of the gas and the changes in saturation are visualized at the pore scale level. This does not only allow us to obtain in situ evidence and the quantification of trapped gas saturation, but also to characterize other impacting factors such as capillary effects that may influence the trapping behaviour.

Our experiments reproduce the behaviour reported in the literature [7] that even though brine is fully saturated with gas when injected in the core, the trapped gas still dissolves within the pores. The high resolution (pore scale resolution) of imaging, allows us to discriminate two different regimes: (1) the displacement, which is dominated by capillary trapping where the gas pathways from inlet to outlet are disconnected by snap-off, and (2) the dissolution, which is caused by Ostwald ripening, which has been largely under-estimated and plays an important role on changing the gas dynamic behaviour.

Minkowski functionals provides us with a useful tool to estimate the upper and lower bounds on the trapped/residual gas saturation. Based on the differences in the displacement/dissolution regime and the observation of the pore scale dissolution dynamics and impact on connectivity, we discriminate the flow regimes using Minkowski functionals by calculating the Euler characteristic, interfacial area and the corresponding curvature. Euler characteristic can be used to distinguish whether the number of the gas phases changes. Interfacial area can be used to check how quick the dissolution goes inside of the sample. Since the gas ganglia size is becoming more and more spherical, which could be reflected by the curvature. Using this workflow, displacement and dissolution stages can be distinguished clearly.

In the dissolution regime, we find that the dissolution rate for all 3 gases gasses scales well with the product of solubility and diffusion coefficient. In the capillary trapping regime, although we have performed only a limited number of experiments, we found systematic differences between CH_4 and H_2 than for compressed air/N_2. While additional experiments are currently underway, some of them extended towards a larger scale (at core plug/Darcy scale vs. the pore scale shown here), if confirmed, this has potentially significant implications in terms of whether compressed air/N2 (widely used currently in SCAL in the industry) is the appropriate gas to be used in laboratory for relperms and trapping gas experiments.

Acknowledgements

Rouhi Farajzadeh is gratefully acknowledged for helpful discussions, particularly with respect to the scaling of the dissolution slope with the product of Henry's constant and molecular diffusion coefficient.

References

1. S. Bachu, Environmental Geology **44.3** (2003): 277-289.
2. S. M. Benson, D.R. Cole. Elements 4, no. 5 (2008): 325-331.
3. R. Juanes, C. W. Christopher, M. L. Szulczewski. Transport in porous media 82 (2010): 19-30.
4. M.J. Blunt. *Multiphase flow in permeable media: A pore-scale perspective* (Cambridge university press, 2017)
5. Ø. Bull, F. Bratteli, J.K. Ringen, K. Melhuus, A.L. Bye, J. E. Iversen, 2011, Paper SCA2011-03 presented at the International Symposium of the Society of Core Analysts, Texas, USA, 1-12. (2011)
6. A.W. Cense, H.A. van der Linde, N. Brussee, J. Beljaars, A. Schwing. Paper SCA2014-009 presented at the International Symposium of the SCA held in Avignon, France (2014)
7. A.W. Cense, J. Reed, P. Egermann. Paper SCA2016-023 presented at International Symposium of the Society of Core Analysts held in Snowmass, Colorado, USA, 21-26 (2016)
8. T. M. Geffen, D.R. Parrish, G. W. Haynes, and R. A. Morse. Journal of Petroleum Technology 4, 02(1952), 29-38.
9. D.K. Keelan, V.J. Pugh. Society of Petroleum Engineers Journal, 15(02), 149-160 (1975)
10. D.C. Crowell, G.W. Dean, A.G.Loomis. Efficiency of gas displacement from a water-drive reservoir, 6735, US Department of the Interior, Bureau of Mines. (1966)
11. J. J. Pickell, B. F. Swanson, W. B. Hickman. Society of Petroleum Engineers Journal 6.01 (1966): 55-61.
12. C.S. Land. Society of Petroleum Engineers Journal, 8(02), 149-156 (1968)
13. C.S. Land, Society of Petroleum Engineers Journal, 11(04), 419-425 (1971)
14. J. Kleppe, P. Delaplace, R. Lenormand, G. Hamon, E. Chaput. Paper SPE-38899-MS presented at the SPE Annual Technical Conference and Exhibition, San Antonio, Texas, US (1997)
15. K. Suzanne, G. Hamon, J. Billiotte, V. Trocme. Paper SPE-84038-MS presented at the SPE Annual Technical Conference and Exhibition, Denver, Colorado, US (2003)
16. L.C. Long. Paper WPC-10134 presented at the 6th World Petroleum Congress, Frankfurt am Main, Germany (1963)
17. A. Firoozabadi, G. Olsen, T. van Golf-Racht. Paper SPE-16355-MS presented at the SPE California Regional Meeting, Ventura, California, US (1987)
18. M.H. Holtz. Paper SPE-75502-MS presented at the SPE Gas Technology Symposium, Calgary, Alberta, Canada (2002)
19. M.J. Blunt, B. Bijeljic, H. Dong, O. Gharbi, S. Iglauer, P. Mostaghimi, A. Paluszny, C, Pentland. 2013. Advances in Water resources, 51, 197-216 (2013)
20. D. Wildenschild, A.P. Sheppard. Advances in Water resources, 51, 217-246 (2013)
21. S. Berg, H. Ott, S.A. Klapp, A. Schwing, R. Neiteler, N. Brussee, A. Makurat, L. Leu, F. Enzmann, J.O. Schwarz, M. Kersten. Proceedings of the National Academy of Sciences, 110(10), 3755-3759 (2013)

22. C.H. Pentland, E. Itsekiri, S.K. Al Mansoori, S. Iglauer, B. Bijeljic, M.J. Blunt. Society of Petroleum Engineers Journal, 15(02), 274-281 (2010)
23. S. Iglauer, A.Paluszny, C.H. Pentland, and M.J. Blunt. Geophysical Research Letters, 38(21) (2011)
24. K. Chaudhary, M. Bayani Cardenas, W.W. Wolfe, J.A. Maisano, R.A. Ketcham, P.C. Bennett. Geophysical Research Letters, 40(15), 3878-3882 (2013)
25. S. Berg, R. Armstrong, H. Ott, A. Georgiadis, S.A. Klapp, A. Schwing, R. Neiteler, N. Brussee, A. Makurat, L. Leu, F. Enzmann. Petrophysics-The SPWLA Journal of Formation Evaluation and Reservoir Description, 55(04), 304-312 (2014)
26. Y. Gao, Q. Lin, B. Bijeljic, M.J. Blunt. Physical Review Fluids, 5(1), p.013801 (2020)
27. Y. Gao, A.Q. Raeini, M.J. Blunt, B. Bijeljic. Physical Review E, 103(1), 013110 (2021)
28. M. Rücker, S. Berg, R.T. Armstrong, A. Georgiadis, H. Ott, A. Schwing, R. Neiteler, N. Brussee, A. Makurat, L. Leu, M. Wolf. Geophysical Research Letters, 42(10), 3888-3894 (2015)
29. Y. Gao, A. Georgiadis, N. Brussee, A. Coorn, H. van Der Linde, J. Dietderich, F.O. Alpak, D. Eriksen, M. Mooijer-van Den Heuvel, M. Appel, T. Sorop. Oil & Gas Science and Technology-Revue d'IFP Energies nouvelles, 76, 43 (2021)
30. Y. Gao, T. Sorop, N. Brussee, H. van der Linde, Hilbert, A. Coorn, M. Appel, S. Berg. Petrophysics 64, 368–383 (2023)
31. W. Burger, M.J. Burge. *Digital image processing: an algorithmic introduction using Java*. (Springer, 2016)
32. J. Benesty, J. Chen, Y. Huang, I. Cohen. In Noise reduction in speech processing, 1-4, Springer, Berlin, Heidelberg (2009)
33. R. Farajzadeh, S. Vincent-Bonnieu, N. Bourada Bourada. Journal of Soft Matter, 1 (2014)
34. K. Xu, R. Bonnecaze, M. Balhoff. Physical review letters, 119(26), 264502 (2017)
35. K. Xu, Y. Mehmani, L. Shang, Q. Xiong. Geophysical Research Letters, 46(23), 13804-13813 (2019)
36. S. Berg, Y. Gao, A. Georgiadis, N. Brussee, A. Coorn, H. van der Linde, J. Dietderich, F.O. Alpak, D. Eriksen, M. Mooijer-van den Heuvel, J. Southwick. Petrophysics-The SPWLA Journal of Formation Evaluation and Reservoir Description, 61(02), 133-150 (2020)
37. J. E. McClure, R.T. Armstrong, M. A. Berrill, S. Schlüter, S. Berg, W. G. Gray, C.T. Miller. Phys. Rev. Fluids 3(8), 084306 (2018)
38. W. Nagel, J. Ohser, K. Pischang. Journal of microscopy, 198, pp.54-62 (2000)
39. J.E. McClure, T. Ramstad, Z. Li, R.T. Armstrong, S. Berg. Transport in Porous Media, 133, pp.229-250 (2020)
40. G. Taubin. In Proceedings of the 22nd annual conference on Computer graphics and interactive techniques, pp. 351-358 (1995)
41. D. Singh, H. A. Friis, E. Jettestuen, J. O. Helland, Transport in Porous Media 145, 441-474, 2022.
42. D. Singh, A. A. Friis, E. Jettestuen, J. O. Helland, Journal of Colloid and Interface Science 647, 331-343, 2023.
43. Y. Zhang, B. Bijeljic, Y. Gao, S. Goodarzi, S. Foroughi, M. J. Blunt, Geophysical Research Letters 50, e2022GL102383, 2023.
44. S. Goodarzi, Y. Zhang, S. Foroughi, B. Bijeljic, M. J. Blunt, International Journal of Hydrogen Energy 56, 1139-1151, 2024.
45. S. Goodarzi, G. Zhang, B. Bijeljic, M. J. Blunt, International Journal of Hydrogen Energy 114, 475-485, 2025.